

Gamma Imaging: Developing a Non-Invasive Analysis Technique for use in Archaeological Research

Sophia Baker (and Aidan Jackson)
L3 Laboratory Project: Epiphany Term 2020
Submitted: 22-04-2020

This work investigates the feasibility of gamma imaging as a non-invasive analysis technique for use in archaeological research, utilising the gamma ray emission of Cs-137 and a high purity germanium (HPGe) detector to image medieval human femur samples from Durham Market Place. A practical method is developed; the mechanics of the apparatus, and the elimination of background radiation and other sources of uncertainty are considered. A compromise between resolution and measurement duration is made. We discuss the workings of the HPGe detector, calculating its efficiency for six gamma photopeak energies and hence finding the energy-efficiency relationship. A Gaussian blur low-pass filter is applied to the images produced to remove anomalous high frequency components. We test the ability of the method to yield numerical data by determination of the linear attenuation coefficient, μ , of cortical bone, finding $\mu = (0.058 \pm 0.004) \text{ cm}^{-1}$, 61% of the literature value. This discrepancy is put down to unsuitability and oversimplification of method, as well as deviations between the modern bone described by literature and our medieval bone. Our method's limitations are discussed, and improvements to it are proposed.

I Introduction

When an unstable atomic nucleus undergoes radioactive decay, there are some cases in which the resultant nuclide is left in an excited state. When this nuclide “falls” to the ground state, i.e. undergoes de-excitation, a photon, of energy ϵ equal to the discrete difference in energy between the excited and ground states, is emitted. This is gamma radiation [1].

Gamma radiation has applications in a diverse range of fields, particularly for the investigation of samples which require non-invasive analysis. They are the shortest wavelength electromagnetic wave, and therefore highest energy and most penetrating. Archaeological samples which are difficult to scan using x-rays have previously instead been imaged using gamma rays, due to gamma’s similar nature but higher penetration capabilities [3].

Not all nuclei decay directly to the ground state, and so multiple energies of gamma ray can be emitted, or other modes of decay and emission can occur, e.g. β^- . Figure 1 shows the decay scheme of Cs-137, the isotope we use in the imaging process.

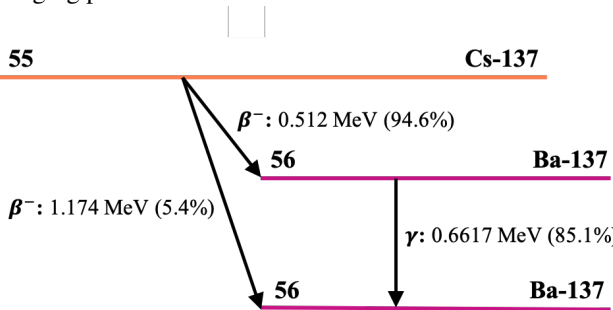


Figure 1: The decay scheme of Cs-137. Note the two paths by which Cs-137 can decay to the final stable isotope Ba-137: either via β^- decay followed by the emission of a gamma photon, or via a single, higher energy β^- decay. The type of transition is given in bold, followed by its energy, and its percentage intensity (bracketed). Atomic number is given in bold. There is a third decay path from Cs-137 to Ba-137, resulting in a gamma photon of energy 283.5 keV, which we ignore here as it is of negligible intensity ($5.8 \times 10^{-4}\%$) [2].

In this work, we investigate the viability of gamma techniques for the imaging of archaeological human remains. We

build our own imaging apparatus, and use it to produce images of three human femur bone fragments of medieval origin, excavated from Durham Market Place. Computational techniques are then employed to apply various filters to these images to improve contrast and other aesthetic factors, and to distinguish between regions of bone and of empty space.

With these regions identified, we can measure the attenuation coefficients of cortical bone for these particular fragments using the image data. The linear attenuation coefficient, μ , gives the thickness of material radiation must pass through to experience a decrease in intensity of a factor of e , i.e. it is characterised by the amount of radiation that can penetrate a unit distance of material. The relationship between the intensity of radiation before and after passing through the material, I_0 and I_x respectively, the thickness of the material in question, x , and μ is given by:

$$I_x = I_0 \exp(-\mu x). \quad (1)$$

An alternative form of equation 1 is:

$$I_x = I_0 \exp(-\mu_m \rho x), \quad (2)$$

substituting μ , which has units of inverse length m^{-1} , for the product of the mass attenuation coefficient, μ_m , with units $\text{m}^2 \text{kg}^{-1}$, and density, ρ , with units of kg m^{-3} [4]. The attenuation coefficient has contributions from scattering and absorption components.

We calculate μ by taking I_0 to be the mean count rate for the images’ empty regions and I_x to be the mean count rate for sets of pixels corresponding to areas of known bone thickness and type, as measured in the lab. These values can then be averaged to give one linear attenuation coefficient. As the density of bone varies, even within the same sample, the mass attenuation coefficient would be difficult to pinpoint.

We weigh the bones and measure their dimensions. Approximating the bones as cylindrical shells, we estimate their volume, so as to estimate their density, ρ_{\approx} . Knowing ρ_{\approx} allows the calculation of an approximate attenuation coefficient μ_{\approx} , rather than relying on literature values for ρ , which is given for modern bone. Discrepancy between our experimental μ , μ_{\approx} and μ given in literature can then be discussed contextually.

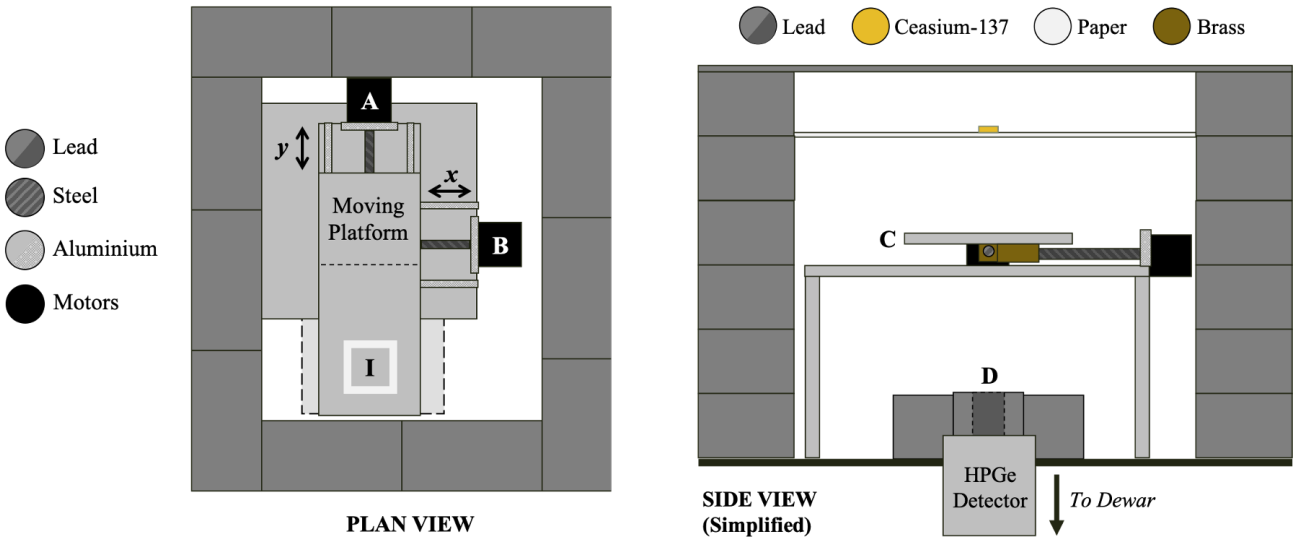


Figure 2: The left diagram shows a plan view of the moving platform and imaging area, to which samples are secured. Motor *A* moves the platform in the *y* direction, and motor *B* moves the platform in the *x* direction. As the platform moves, *B* remains stationary but *A* moves with it. The imaging area *I* has dimensions (48 ± 1) mm by (57 ± 1) mm. Note the overhanging platform; this is to avoid attenuation by the brass components of the screw mechanism by which the platform is moved. This larger area also allows for the imaging of larger samples. To the right is a simplified schematic showing a cross-sectional view of the imaging set-up from one side. *C* is the moving platform; *D* is the lead collimator (to be discussed in detail in section II.5). Each lead brick is (50 ± 5) mm tall (the uncertainty largely coming from defects in size of individual bricks) meaning that the source is (250 ± 11) mm above the workbench and (232 ± 11) mm above the detector; the detector cap protrudes (15 ± 1) mm above the workbench and is 3 mm thick (see the HPGe specification sheet in the appendix). The position of the collimator block is represented by dashed outlines in the plan view and is coloured lighter for clarity.

II Methodology

II.1 Experimental Set-Up and Method

We image samples by placing them on a moving platform between a sample of Cs-137, a gamma ray source, and high purity germanium (HPGe) gamma ray detector, and measuring the detected count rate, \dot{N} , as different parts of the platform pass over the detector. When the sample passes between the source and detector, it attenuates a proportion of the emitted gamma radiation, reducing \dot{N} . Measurements are made with the sample at different positions in space, and hence a map of \dot{N} is produced. This map is the initial image. Details of the experimental setup are shown in figure 2.

The moving platform is moved in *x* and *y* by two motors, one for each direction. These motors turn the two steel screws, which move the platform in the desired direction by a small increment. We choose our imaging area such that it is 105 increments wide. The number of pixels in each direction, number of increments between each pixel, and counting time at each pixel are inputted via a LabView GUI. To correspond with our 105 increment wide imaging area, and as a compromise between resolution and imaging time, we choose to take 35 by 35 pixel images, with a difference in position of three increments between each site of measurement (i.e. each pixel in the final image). We find 60 seconds of counting time per pixel provides adequate contrast. Each image takes 20 hours 25 minutes to produce (not including filters or analysis).

Due to the pulsing nature of the motors, the sample must be secured on the moving platform so that it does not shift during measurements. Each bone fragment is placed in a custom made paper casing, padded with paper tissue

to prevent movement. The paper casing is secured to the imaging area using blu-tac.

The apparatus is mounted on an aluminium table, such that the motors and screw mechanisms are supported directly, and the moving component, onto which the imaging area is marked, protrudes over empty space. This is to avoid the imaging of other components of the mechanical set-up, namely the brass blocks through which the steel screws are threaded. Aluminium and steel have relatively low attenuation coefficients, so do not show in images. However, such are the attenuation properties of brass that the blocks were clearly visible in early test images (see appendix).

The alternative to the construction of the protruding section of the moving platform would have been to take a “background” image of just the brass blocks and other components and use this to account for their appearance in final images. However, this would be a much more complicated and time consuming process than simply building an extension to the apparatus.

We determine the placement of the platform and hence the location of the imaging area by placing a small lead block in the corner of our desired area. We then take test images of the block, repositioning the platform until the block appears in the desired corner of the image. In this work, the images produced are mirror images due to the direction in which measurements were taken, but this could have been avoided by repositioning equipment.

As the imaging area itself is limited in size, larger samples are imaged in sections. Markings are made along the side of the paper casings such that the end of one section corresponds with the start of the next. The addition of the extension to

the moving platform further facilitates the imaging of larger samples by providing more space upon which to place them.

Ideally, we would image using a gamma point source, for efficiency reasons, but this is not possible. However, steps are taken to make our gamma source more point-like. The source radiates gamma radially in a sphere, so distance and intensity of radiation follow an inverse square law, i.e. the density of gamma waves decreases with distance. Therefore, to replicate a point source, the source should be high enough above the detector that only gamma rays travelling in one direction (downwards) are detected. In the laboratory, compromise must be made between height and quality of point source emulation.

For reasons of safety and convenience, the lead shielding cannot be built too high. The height of the aluminium table onto which the apparatus is clamped is therefore chosen to be (160 ± 5) mm, a height deemed appropriate with respect to that of the shielding. The aluminium table's adjustable screw feet allow us to compensate for the slight incline of the workbench, and are the main source of uncertainty in the table's height.

Additionally, with increased height and smaller solid angle “seen” by the detector comes a decrease in detected count rate, and so in order to measure sufficient counts to construct a clear image, more time must be spent on each measurement. As the imaging process is already long, this is not ideal, and so another compromise must be struck.

II.2 Radiation Safety Measures

Radioactive sources pose dangers to us as experimentalists via exposure, especially when they are unshielded. To avoid unnecessary exposure to radiation, lead brick shielding of thickness (75 ± 5) mm is built around the experiment. Care must be taken when handling lead; gloves are worn during all contact to protect from its toxicity, and as each brick weighs over 6 kg, appropriate lifting techniques must be employed (e.g. lifting only one brick at a time, using two hands).

At a distance of X m from a radioactive source, the dose rate, \dot{D} , is given by comparison with a known \dot{D} . Here we use \dot{D} measured 1m away from a Co-60 source, with values as given in [5]:

$$\dot{D} = \dot{D}_{Co} \frac{\Sigma E}{\Sigma E_{Co}} \left(\frac{1}{X} \right)^2 \frac{A_0}{A_{Co0}}, \quad (3)$$

where ΣE is the sum of energies, i.e. the photopeak energy, and A_0 is the source's activity, or strength. ΣE_{Co} and A_{Co0} are those values for Co-60. Note that A_0 is an approximation using the source's activity as it was when last measured, and the actual source strength decreases with time.

Our Cs-137 source, of strength $10 \mu\text{Ci}$, and must pass through approximately 20 mm of air, (75 ± 5) mm of lead, and another 1 m of air before it reaches the closest experimentalist's workstation. In the absence of lead shielding, with gamma rays travelling solely through air, at distance 1.25 m from the source the dose of radiation received is $0.0210 \mu\text{Svhr}^{-1}$.

However, with the inclusion of the lead brick shielding, which

has $x = (75 \pm 5)$ mm and $\mu_{Pb} = 1.27 \text{ cm}^{-1}$ (see appendix), this dose decreases further.

We first calculate the dose rate at the interior of the shielding (approximately 20 mm from the source) from equation 3. The change in dose rate due to the lead is then calculated using equation 1.

We find that the lead shielding reduces the dose of radiation from $0.822 \mu\text{Svhr}^{-1}$ to $6.00 \times 10^{-5} \mu\text{Svhr}^{-1}$, a decrease of 99.99%. Assuming we spend 90 hours in the lab, that a source is in position for all of this time (an overestimate), and that we are constantly next to the apparatus, a total dose of 5.40 nSv is received. This is negligible versus of the annual dose limit for the public, 1 mSv [5]. The 1 m between the apparatus and workstations further decreases this estimated received dose.

The bone fragments we image do not become radioactive upon exposure to radiation.

II.3 About our Test Samples

The samples investigated in this work are human remains and as such must be treated ethically and with care and respect. They are stored out of sight and only removed from their bag and box for the taking of measurements. We name the samples DMP1, DMP2 and DMP3, where DMP stands for Durham Market Place and the ascending numbers correspond to ascending length. There are two identifiable types of bone in the DMP sample set, cortical and cancellous.

Cortical bone is a solid structure, providing more rigidity and strength than cancellous. The femur is primarily a hollow tube of cortical bone (the hollow region, the diaphysis, would contain bone marrow in living bone). However, this changes at the epiphyses (the ends of the femur that connect to the hip and knee), where cancellous bone, also known as trabecular bone, becomes the predominant constituent. It is comprised of a honeycomb-like lattice of bony trabeculae, giving it a porous, “spongy” consistency. In living bone, the pockets in the “sponge” structure are occupied by other tissue, but this has decayed in archaeological samples. Cancellous bone is usually encased in cortical bone; however, as our samples are fragmented, some trabecular structure is exposed [6][7].

Assuming that a sample has a constant attenuation coefficient throughout, the resultant map of counts acts as an image of the sample from which its shape and size is obvious. However, the three human femur bone fragments imaged in this work have hollow sections and are of varying composition, as described. We will therefore be unable to produce a 3-D representation of the bone from the map of count rates alone. For example, a hollow region with two “walls” of thickness 5 mm will allow through approximately the same number of counts as a sheet of thickness 10 mm. However, we know the size of our samples, and so if we also know the approximate value of the expected attenuation coefficient, which can be found in literature, it can be determined whether a section of bone is hollow. This is possible by comparing the expected thickness x , which we can calculate by rearranging equation 1, to the sample's true size.

II.4 The High Purity Germanium Detector

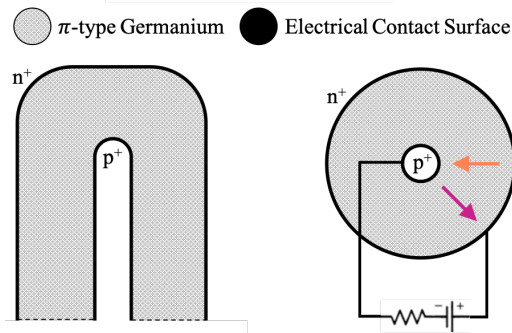


Figure 3: Simplified diagram of the bulletised closed-ended coaxial HPGe detector used in this work. For more detail see the appendix. The orange and pink arrows represent the movement between the electrical contact surfaces of holes and electrons respectively. The inner contact surface is composed of germanium and boron ions, and the outer germanium and lithium ions, so as to give them opposite charges. This makes our detector a *p*-type HPGe [8].

The ORTEC HPGe gamma ray detector counts gamma photons and hence measures \dot{N} . HPGe detectors belong to the semiconductor class of detectors; silicon detectors also fall into this category. We choose a HPGe detector for its high efficiency and precision, which are a result of the germanium's extreme purity (the impurity concentration can be as low as 10^{10} atoms/cm³, or 1 part in 10^{12}). High purity is easier to achieve for germanium than silicon due to the nature of the manufacturing process. The lower boiling point of germanium (1232 K versus silicon's 1683 K) allows for the easier exclusion of impurities in the refining process. High purity germanium is manufactured via zone refining, a process in which localised heat is applied to bulk germanium, and the resultant molten germanium, in which impurities are most soluble, and so is where they predominantly gather, is discarded. This first step reduces the impurity concentration to 10^9 atoms/cm³. Large, purer crystals are then grown from this germanium "feedstock." Our detector consists of one of these crystals in a bulletised closed-ended coaxial form, as shown in figure 3 [8].

HPGe detectors have a depletion depth of the order of 10^{-2} m, much greater than other types of detector, allowing for the total absorption of higher energy photons, and higher detector efficiency [9].

The detector must be at liquid nitrogen temperatures (approximately 77 K) to prevent the destruction of the germanium crystal by the sudden influx of voltage applied (we use 2.5 kV). The low temperature also helps reduce thermal noise, i.e. the thermal generation of unwanted charge carriers. To maintain these conditions, the detector is mounted in a dewar of liquid nitrogen.

When ionising radiation is incident on the detector, a number of charge carriers proportional to the radiation energy are "freed," i.e. a number of electron-hole pairs are created, with the holes created in the valence band and electrons transferred to the conduction band of the germanium. These electrons and holes travel to the electrodes, as shown by the arrows in figure 3, under the influence of the electric field created by

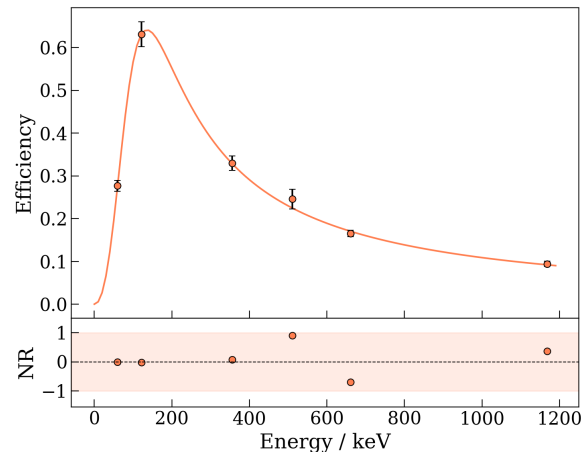


Figure 4: Plot of intrinsic efficiency against energy for the HPGe detector as measured in the laboratory. All normalised residual points (NR) lie within ± 1 (shaded region), as required for a good fit [10]. However, $\chi^2_\nu = 5.72589585752 \times 10^{-5}$ for this fit, implying the opposite. This is the result of overestimated errors. Due to the small number of points, we will not comment on the residuals' shape. The points, left to right, correspond to Am-241, Eu-152, Ba-133, Na-22, Cs-137 and Co-60. We choose to use Cs-137, despite its lower η , due to its decay scheme's relatively simplicity (see figure 1).

the applied voltage; information about the incident radiation's energy is carried to the relevant instruments in the resultant electrical pulse [9]. In this work, signals from the HPGe are amplified and split between two PCs. One of these PCs acts with a multichannel buffer (MCB) and the MAESTRO software package to generate and display spectra. The other is host to a LabView program which both controls the moving platform's position and takes input from the detector to generate images [8].

Figure 4 shows the energy-efficiency relationship for our HPGe detector with no collimator fitted. Each energy and its corresponding efficiency is obtained by measuring the count rate at the energy of the gamma peak of a different radioactive source, and calculating the expected count rate. For these measurements the sources were placed at a distance $R = (315 \pm 5)$ mm above the detector cap. Our detector has a diameter of 53.3 mm (see the HPGe specification sheet in the appendix).

We calculate the intrinsic efficiency, denoted η , as follows:

$$\eta = \frac{\dot{N}_{total} - \dot{N}_{bg}}{\dot{N}_{true}} \quad (4)$$

where \dot{N}_{total} is the total count rate in the energy range of interest with the source present, \dot{N}_{bg} is count rate in the same range with no source present, and \dot{N}_{true} is the calculated count rate:

$$\dot{N}_{true} = A_0 e^{(-\ln 2)(t/t_{1/2})} \gamma F, \quad (5)$$

where A_0 is the activity of the source, t is its age, $t_{1/2}$ is its half-life, and γ is the gamma fraction, the intensity of gamma radiation received at photopeak energy (see appendix for their values) [1]. F is a geometric factor dependent on the detector's radius, $r = \frac{d}{2}$, and its distance from the gamma source, R :

$$F = \frac{4\pi R^2}{\pi r^2}. \quad (6)$$

where d is the detector diameter. With a collimator, we assume that $d = D$, the diameter of the collimating aperture.

The energy-efficiency relationship is given by:

$$\eta = \frac{ae^b}{c + de^e}, \quad (7)$$

with efficiency given by η , energy by ϵ , and parameters as found via χ^2 minimisation (a, b, c, d and e equal to $0.193 \text{ eV}^{-2.24}$, 2.24 , 5880 , $9.74 \times 10^{-4} \text{ ev}^{-3.33}$ and 3.33 respectively). This relationship is adapted from [11].

We assume that $\dot{N}_{\text{total}} - \dot{N}_{\text{bg}}$ will change by the same factor as \dot{N}_{true} if D and R are varied, and hence that this efficiency curve applies throughout this work.

II.5 Introducing Collimators

Collimators are used to reduce the area upon which gamma photons are incident and therefore the solid angle “seen” by the detector, aiding the simulation of a point source. We test three collimators of differing aperture size before choosing one to use when taking our final images. The collimators are composed of two lead bricks (of the same dimensions as those shielding the apparatus), each with a semi-circular cut-out section to fit over half of the (15 ± 1) mm protrusion of the HPGe detector through the workbench, and another, smaller semi-circular cut-out but this time passing straight through the brick, as seen in figures 2 and 5. These two halves are then placed together such that the semi-circular cut-outs join to make concentric circles. Three hollow cylindrical “plugs,” each of different internal diameters D , can be inserted into the second cut-out so as to adjust aperture size. Their outer radii match the radius of the hole into which they are placed.

The upper section of figure 6 shows \dot{N} and the change in this with the presence of a lead block for each of our three apertures. It appears that the 30 mm aperture will provide the most contrast due to the large number of counts detected in the unobstructed region versus the absence of counts caused by the lead block, and that the 10 mm aperture provides the least contrast, as the number of counts detected in the unobstructed region is already low. However, the percentage differences between the count rates with the block and without for each aperture are similar, with the placement of the lead block causing a decrease in count rate of approximately 95%.

We take the gradient of the fall (and subsequent rise) in \dot{N} corresponding to the lead block for each aperture. The gradient corresponding to the 30 mm aperture has the greatest absolute average, $4.37 \text{ counts} \cdot \text{s}^{-1} \cdot \text{pixel}^{-1}$, implying the most rapid change in count rate with the introduction of the lead block, i.e. high contrast. The values for 20 mm and 10 mm are $2.63 \text{ counts} \cdot \text{s}^{-1} \cdot \text{pixel}^{-1}$ and $2.00 \text{ counts} \cdot \text{s}^{-1} \cdot \text{pixel}^{-1}$ respectively.

Having established that contrast is aperture size dependent, we now consider the resolution achieved using each aperture. We have established that the block’s width, (20 ± 1) mm corresponds to approximately 12 pixels. This number of pixels is exactly matched by the width of the block’s “shadow” on the image (purple region) taken with the 10 mm collimator,

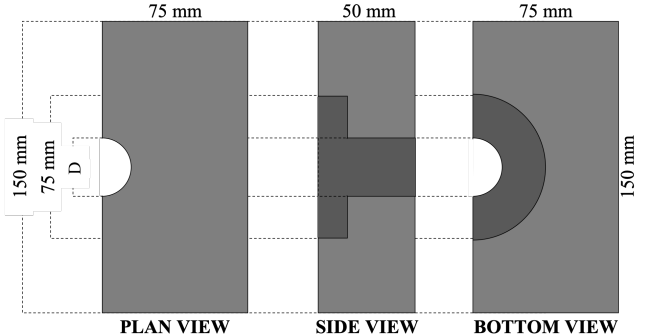


Figure 5: Diagram to show one half of the lead collimator device. D is the diameter of the collimator’s aperture, with possible values of (10 ± 1) mm, (20 ± 1) mm and (30 ± 1) mm. D is varied by inserting “plugs” of different aperture size. Darker areas represent cut-away parts of the collimator. Where not quoted, errors on the measurements shown on this diagram are ± 5 mm.

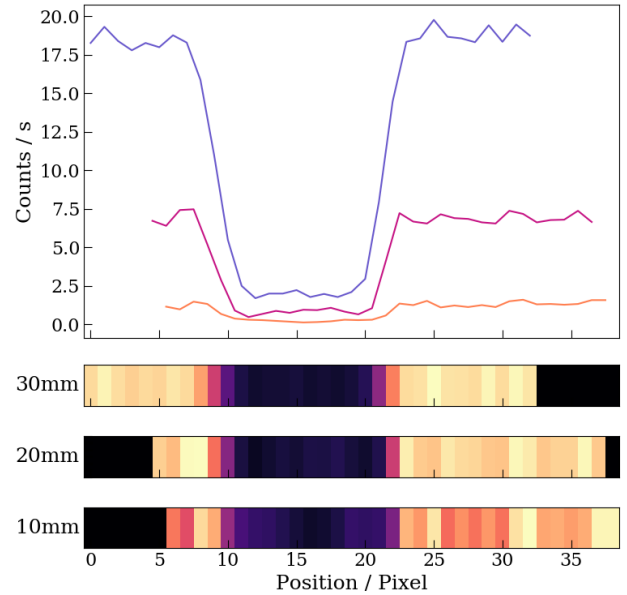


Figure 6: Plots and images to show the count rate over distance when a lead block is placed in the imaging area for each of the three collimator plugs. The purple line corresponds to the 30 mm aperture, pink to 20 mm, and orange to 10 mm. The plots for the latter two aperture sizes have been spatially shifted so as to correct for deviations in block placement and allow for easier comparison of the “shadows” cast by the block. Each set of data is a single row of 33 pixels, corresponding to (57 ± 1) mm. The block is a square (20 ± 1) mm wide, so in a perfect image would correspond to approximately 12 pixels. Note that the single row of pixels has been vertically elongated for clarity, and that the images are only for spatial comparison, as **colour maps are not to the same scale**. Refer to the main plot for any comparison of count rates.

whereas the “shadows” corresponding to the block in the other two images are more “smudged,” and despite their higher contrast, it is more difficult to define the block’s edge, i.e. resolution is lower. We therefore select the 10 mm collimator for our final imaging, increasing the measurement time accordingly to account for the lower incident count rate.

It is worth noting that if the aperture is too small, resolution will decrease due to diffraction effects. However, for gamma radiation with $\epsilon = 661.7$ keV, diffraction effects are usually of no consequence [12].

II.6 Correcting for Background Radiation

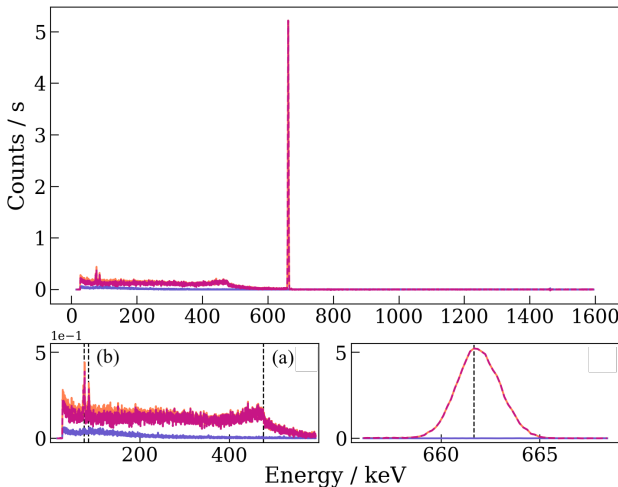


Figure 7: The gamma ray energy spectrum as measured in the laboratory for Cs-137 (with no sample in place). The top subplot shows the whole spectrum measured; the bottom right shows only the Cs-137 gamma photopeak, and the bottom left shows in more detail (a) the Compton edge and (b) peaks corresponding to x-rays emitted by the lead shielding upon excitation by beta radiation. Each of these energies is marked with a dashed black line. The total measured spectrum, background spectrum, and corrected spectrum (obtained from the difference between the former) are shown in solid orange, solid purple and dashed pink respectively.

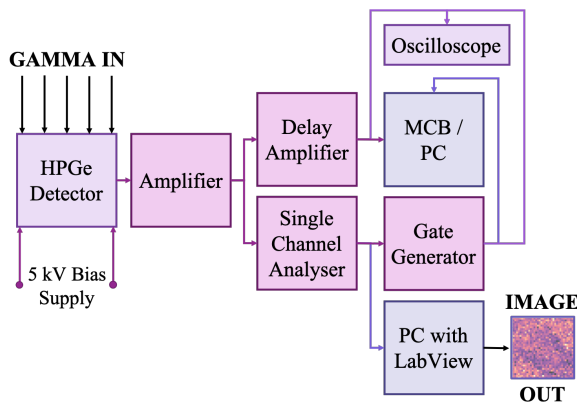


Figure 8: Block diagram showing the flow of information through the experimental setup; The detector is supplied with 2.5 kV from a 5 kV bias supply. The MCB is an interface between the HPGe detector and the PC software package MAESTRO, counting incident gamma photons into channels corresponding to different energies. Amplifier gain determines the energy-channel calibration and is set via two analogue dials (for coarse and fine gain). The higher the gain, the higher the energies given for each channel. The SCA has a similar calibration process. The delay amplifier ensures that signals passing through different components are output at the same time, by delaying the faster signal (by a time step of the order of microseconds). More details given in the appendix.

We are solely interested in counts with energies within the Cs-137 photopeak and their applications in sample imaging. It is therefore necessary to isolate this energy region, so as to avoid the measurement of counts of other energies, particularly those from the Compton edge and x-ray emission peaks.

Compton scattering is the process occurring when only part of a gamma ray photon's energy is transferred to a material (i.e.

to an atomic electron in a material). This lower energy photon continues to scatter and be absorbed by the material until it re-emerges with a final lower energy [13]. These energies are visible in gamma ray spectra as the Compton edge, as shown in figure 7. In this particular case, the scattering will have occurred in the lead shielding or other components of the experimental set-up. Attenuation via Compton scattering is a dominant component of μ for a material, another being photoelectric absorption [13].

Also shown in figure 7, we observe two peaks at energies approximately 75 keV and 84 keV. Lead is known to re-emit x-rays of certain discrete energies upon excitation by other radiation. These observed peaks correspond exactly to its $K\alpha_1$ (74.9694 keV) and $K\beta_1$ (84.936 keV) emission lines as defined in [14], which are the result of electrons moving between energy levels ($n = 2$ to $n = 1$ and $n = 3$ to $n = 1$ respectively) upon the incidence of β radiation emitted by the Cs-137 as it decays to Ba-137 (see figure 1).

A single channel analyser (SCA) is used to select only the Cs-137 photopeak, in combination with a gate and delay amplifier. The arrangement of these components, and other electronics including the detector, is given in figure 8. The SCA must be calibrated to select the correct energy range; this is achieved by selecting an appropriate gain.

We do not take a background image (an image with no sample or source in place, and lead shielding in place around the detector) for subtraction from our final images due to time constraints. The background radiation level shown in figure 7 is low enough at the photopeak energy that we neglect its equivalent during the imaging process.

III Imaging

III.1 Image Processing

The bone fragments are not instantly recognisable in the images produced due to the presence of noise, lack of contrast, and low resolution, as shown in figure 9's section 1A. We therefore apply various filters to our images to increase contrast and eliminate noise, enhancing the bones' definition.

Figure 9's section 1B shows the application of a Median filter of size 5 to our image of DMP2. The Median filter takes the median value of a pixel and its surrounding pixels, reassigning that pixel's value with this new one. The size gives the radius, i.e. the number of pixels, over which the median is taken [15].

The Gaussian blur is shown in figure 9's sections 2A and 2B. Like the Median filter, the Gaussian blurs the image so as to remove noise. Though this comes at the cost of reduced resolution, edges are generally preserved better in a Gaussian blur than in other blurring filters (however, the median filter is more effective for lower levels of Gaussian noise [15]). The Gaussian function is also a Fourier transform of itself, meaning it acts as a low pass filter, removing any high frequency components of the image [16]. This is important as some pixels have anomalously high count rates, due to cosmic rays striking the detector at energies coinciding with the gamma photopeak.

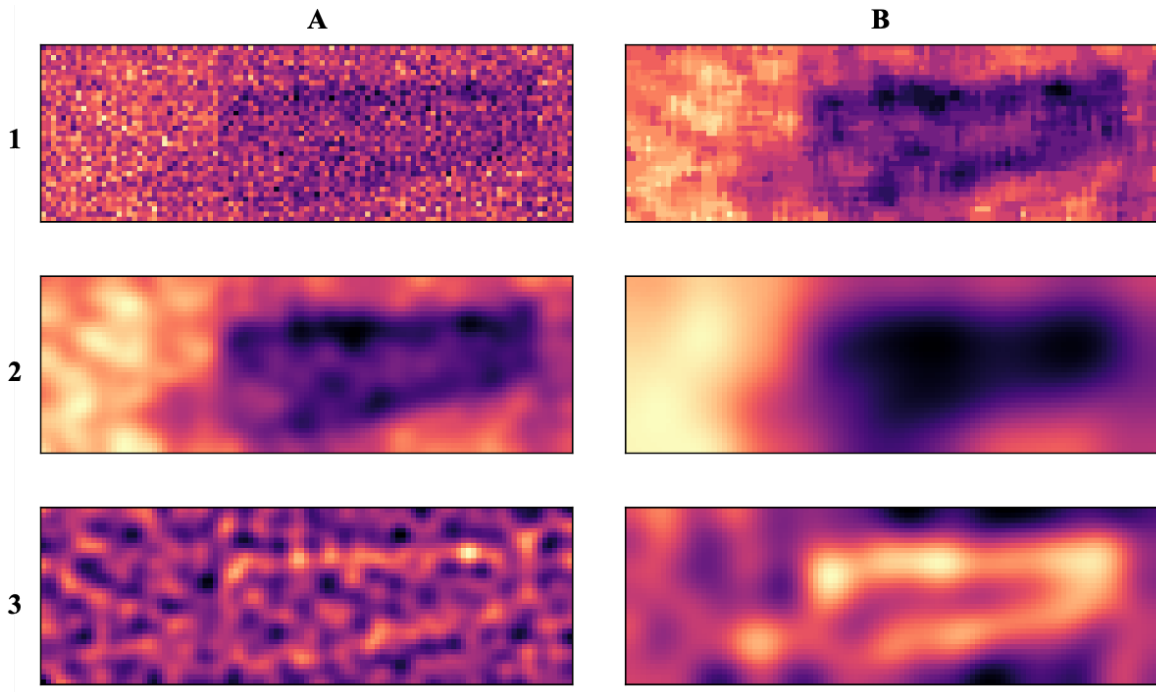


Figure 9: Demonstration of the effect of filters on DMP2. 1A is the original image and 1B is that image with a Median filter (size = 5). 2A and 2B show the application of a Gaussian blur, and 3A and 3B a Laplace-Gaussian filter, both with $\sigma = 2$ and $\sigma = 5$ respectively. As is evident here, the higher σ (or in the case of the Median filter, the larger the size), the more the image is blurred. Colourbars are excluded; as in figure 6, these images are not on the same colour scale, with 3's darkest and lightest regions corresponding to values of $\pm 0.03 \text{ counts} \cdot \text{s}^{-1}$, 1B and 2's corresponding to approximately 1.1 to $1.5 \text{ counts} \cdot \text{s}^{-1}$, and 1A's to approximately 0.75 to $1.75 \text{ counts} \cdot \text{s}^{-1}$.

The 2-D Gaussian function is given by:

$$G(x, y) = \frac{1}{2\pi\sigma^2} e^{-\frac{x^2+y^2}{2\sigma^2}} \quad (8)$$

where σ is the standard deviation of the distribution [17]. For a Gaussian blur, this function is applied to each pixel in the image to give its transformed counterpart. A convolution matrix is constructed from this distribution; this is applied to the original image. Each pixel now has a new value, a weighted average of its neighbouring pixels, with the most weight on the original pixel, and decreasing weight with increasing distance from the original pixel. The larger the value of σ , the broader the range of pixels included, so the greater the blur. [16].

The Laplace-Gaussian filter, as shown in row 3 of figure 9, applies both a Gaussian blur and Laplace transform to an image. This filter is useful for highlighting edges.

III.2 Final Images

A Gaussian blur with $\sigma = 2$ is the most suitable for the enhancement of our images, due to its noise-reduction and edge-preservation properties. Images of DMP1, DMP2 and DMP3, with and without the Gaussian blur, are shown in figures 10, 11 and 12.

These images display some of the samples' recognisable features, e.g. the diagonal breakage at one end of DMP1, and the ridge where DMP2's top layer of cortical bone ceases and exposes its cancellous interior structure. The images also reveal information about the structure of the bone fragments that is not visible without the employment of penetrating radiation, or techniques resulting in sample destruction. DMP1 and DMP2 show clear edges, defined by

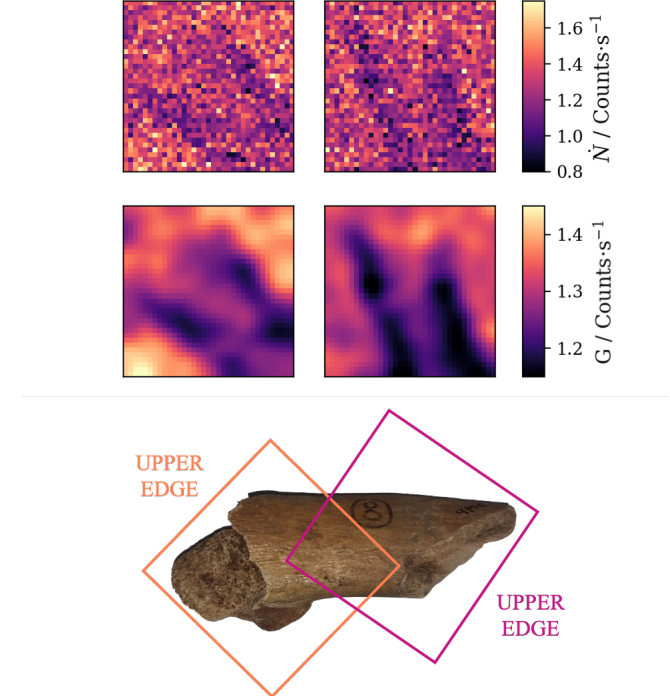


Figure 10: Upper images: the original, unfiltered images of DMP1 (LHS: DMP1A, RHS: DMP1B). Central images: the same images with a $\sigma = 2$ Gaussian blur applied. Lower image: photograph of DMP1. G is the Gaussian transformed version of the original counts. The pink and orange boxes show the areas corresponding approximately to the images above, with the right and left images representing the contents of each box respectively. The two images are not combined due to misalignment of the sample with respect to the imaging area. Laboratory closures due to COVID-19 meant there was no chance of obtaining a new, aligned set of images.

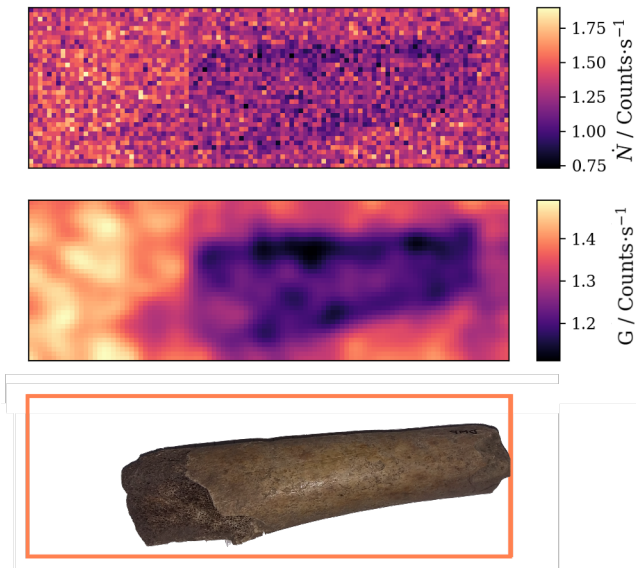


Figure 11: Upper image: the original, unfiltered image of DMP2. Central image: the same image with a $\sigma = 2$ Gaussian blur applied. Lower image: photograph of DMP2; orange box shows the area corresponding approximately to the images above. The fracture edge where the top layer cortical bone ceases and the overall sample thickness decreases significantly is visible in both the photograph and the blurred image.

regions of lower count rate, corresponding to areas of bone which consist of cortical bone with no hollow regions and little or no trabecular structure. DMP3, on the other hand, shows up as an areas of consistently low count rate, implying similar gamma attenuation throughout the fragment. This in turn suggests that DMP3 is not hollow, or at least that any cavity is small. This result is supported by observations of internal structure at the ends of the fragment, from which a predominantly trabecular structure is visible rather than a defined hollow region. It cannot be confirmed that this structure persists to the centre of the fragment without the destruction of DMP3, but our image supports the claim.

IV Further Analysis

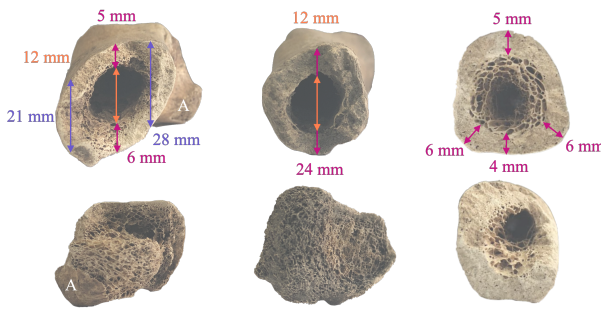


Figure 13: Cross-sections of DMP1, DMP2 and DMP3 (left to right). Though the precision of the callipers used to take the measurements given in this figure was ± 0.01 mm, this level of accuracy was not achieved due to the uneven nature of the bones' surfaces, and we give measurements to larger uncertainties. Due to the different structural properties of each bone samples, it was not possible to take the same measurements on every bone; the diameter of the internal cavity could not be measured for DMP3 due to its predominantly trabecular composition and lack of hollow interior, and for areas with exposed trabecular bone we did not want to damage its fragile structure. Measurements are given to the nearest mm; note that they are not the final x used to calculate μ .

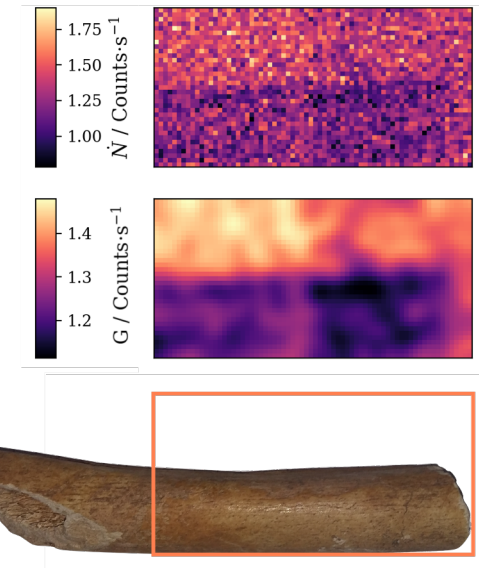


Figure 12: Upper image: the original, unfiltered image of DMP3. Central image: the same image with a $\sigma = 2$ Gaussian blur applied. Lower image: photograph of DMP3; again, orange box shows the area corresponding approximately to the images above. It was not possible to image the entire bone fragment due to time constraints brought on by the cancellation of lab sessions.

IV.1 Finding the Linear Attenuation Coefficient

Rearranging equation 1, we find an expression for the linear attenuation coefficient, μ :

$$\mu = -\frac{1}{x} \ln \left(\frac{I_x}{I_0} \right). \quad (9)$$

For each image, pixels spatially corresponding to empty areas of the image, or to areas of bone of near-constant composition (i.e. solid cortical bone), are selected, and the weighted mean of the count rates, \dot{N}_{WM} , is calculated as follows:

$$\dot{N}_{WM} = \frac{\sum_i w_i \dot{N}_i}{\sum_i w_i}, \quad (10)$$

where \dot{N}_i is the count rate, and $w_i = \frac{1}{\alpha_{\dot{N}_i}^2}$, for the i^{th} pixel [10]. \dot{N}_{WM} calculated for empty areas and areas of bone become the values of I_0 , the average intensity of un-attenuated radiation, and I_x , the average intensity of radiation attenuated by x cm of bone, respectively. These areas of pixels are shown in figure 14. The standard error in the weighted mean, i.e. in I_0 and I_x , is given by:

$$\frac{1}{\alpha_{\dot{N}_{WM}}^2} = \sum_i \left(\frac{1}{\alpha_{\dot{N}_i}^2} \right), \quad (11)$$

where the uncertainty in measured count rate, $\alpha_{\dot{N}_i}$, is:

$$\alpha_{\dot{N}_i} = \dot{N}_i \times \sqrt{\frac{\alpha_{N_i}^2}{N_i} + \frac{\alpha_t^2}{t}}, \quad (12)$$

with the uncertainties in N_i and t , α_{N_i} and α_t , equal to ± 1 count and ± 1 s [10]. We find that $\alpha_{\dot{N}}$ is fairly consistent throughout each image, with uncertainties the $\pm(0.02 - 0.03)$ counts·s $^{-1}$ range for all pixels in DMP3.

An average thickness, x , of bone over the I_x region of pixels is found by measuring the dimensions of the bone with

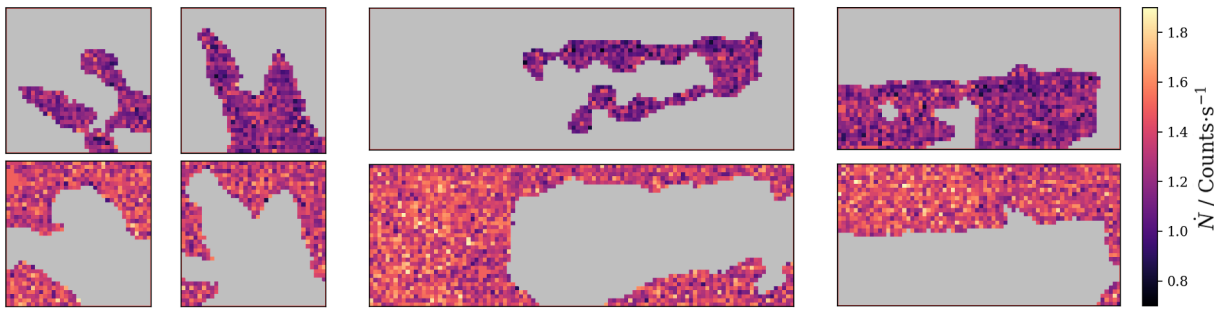


Figure 14: Representations of the pixels involved in the calculation of the weighted mean count rates I_x (upper row) and I_0 (lower row) for DMP1, DMP2 and DMP3 (left to right). Grey represents pixels not included. The selected areas are defined by eliminating all pixels of values which do not fall above or below a numerical threshold of 1.2 counts·s⁻¹ (above and below threshold for background and bone selection respectively). However, we note that the selected regions are not necessarily exclusively bone / background and do not always cover the entire bone / background, as whilst, for example, most background pixels have count rate values above the threshold value, there may be anomalous dark pixels which do not correspond to bone. The pixel selection process uses the Gaussian blur's pixel values, i.e. the low pass filtered values in order to reduce the impact of anomalous pixels. The images above show the corresponding un-filtered pixels, and I_x and I_0 are calculated from these unfiltered values and their uncertainties (in retrospect, calculations using Gaussian blurred pixels with $\sigma < 1$, to avoid high frequencies whilst retaining the original contrast, may have been more appropriate).

vernier callipers. Though the instrument's high precision is lost in this application, as explained in figure 13, it is still an improvement on the alternative of a ruler, which would introduce uncertainty due to parallax. Where possible, multiple measurements of x are made and the mean taken, the uncertainty in x is given as the standard error in the measured values. For DMP1, this results in $x = (25 \pm 4)$ mm. Multiple measurements cannot always be made, so in other cases we also take uncertainty to be ± 4 mm, in an effort to account for (a) the curvature of bone and (b) its potentially varying composition. Uncertainty in μ , α_μ , is calculated via the combination of errors in I_0 , I_x and x , α_{I_0} , α_{I_x} and α_x , for each image [10]:

$$\alpha_\mu = \sqrt{(\alpha_x^\mu)^2 + (\alpha_{I_x}^\mu)^2 + (\alpha_{I_0}^\mu)^2}, \quad (13)$$

where contribution of each of these errors to α_μ , μ , are calculated using the functional approach described in [10]. For example:

$$\alpha_x^\mu = \left(-\frac{1}{x + \alpha_x} \ln \left(\frac{I_x}{I_0} \right) \right) - \mu, \quad (14)$$

with each I_x , I_0 , α_{I_x} and α_{I_0} as given in the appendix. $\alpha_{I_x}^\mu$ and $\alpha_{I_0}^\mu$ are calculated similarly.

Figure 15 shows the μ - ϵ relationship for cortical bone as given by [18]. In order to determine the expected value of μ at the Cs-137 gamma photopeak energy, we fit the μ - ϵ relationship for the region surrounding 661.7 keV using python's `scipy.optimize.curve_fit` function. This yields an almost linear equation:

$$\mu = f\epsilon^g + h\epsilon + i \quad (15)$$

where f , g , h and i are equal to $334 \text{ m}^{-1}\text{eV}^{-1}$, 1.00 , $-334 \text{ m}^{-1}\text{eV}^{-1}$ and 0.311 m^{-1} respectively. A linear fit is also trialled (in response to $g = 1.00$) but it is deemed less suitable by inspection. As errors on the data used were not available, no χ^2 minimisation has been performed.

With the average density of cortical bone, $\rho_{\text{ICRU}} = 1.92 \text{ gcm}^{-3}$ [18], we find the expected value of μ , $\mu_{\text{ICRU}} = 0.154 \text{ cm}^{-1}$

cm^{-1} . Table 1 gives our calculated μ and their uncertainties, along with the percentage difference between μ and μ_{ICRU} .

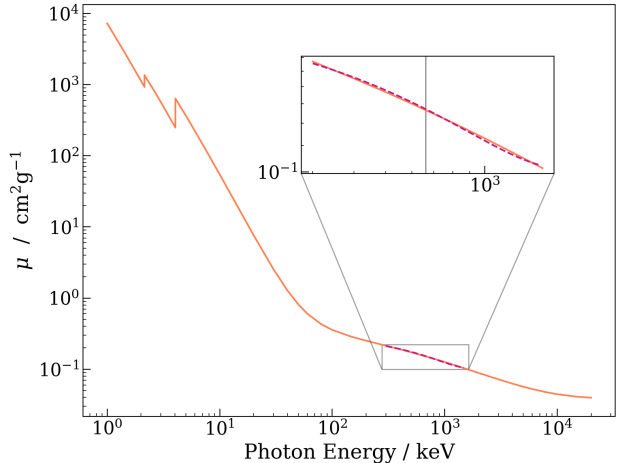


Figure 15: Plot of the x-ray linear attenuation coefficient of cortical bone, μ versus energy, ϵ ; μ is also applicable as gamma ray attenuation coefficients due to the similar nature of these types of radiation. We determine μ at each ϵ by calculating the product of the mass attenuation coefficient, $\mu_{\text{ICRU}}/\rho_{\text{ICRU}}$ at that ϵ , and the density, $\rho_{\text{ICRU}} = 1.92 \text{ gcm}^{-3}$, of cortical bone as given by [18]. The region around our energy of interest, 661.7 keV (marked by the solid grey line in the inset plot), is fitted in order to determine the expected μ at that energy (the value yielded being 0.154 cm^{-1}). The fit, given by equation 15, is plotted in pink, with the μ - ϵ data in orange.

DMP	x / cm	μ / cm^{-1}	%
1A	2.5	0.056 ± 0.007	65%
1B	2.5	0.052 ± 0.007	62%
2	2.4	0.065 ± 0.009	57%
3	2.4	0.07 ± 0.01	55%
Weighted Mean	—	0.058 ± 0.004	61%

Table 1: The attenuation coefficients, μ , for areas of cortical bone with thickness x of approximately 2.5 cm, and the percentage differences (denoted %) between these μ and μ_{ICRU} . We take the weighted mean and standard error, as defined in [10], of the three samples' attenuation coefficients to obtain our final μ .

There are significant discrepancies between our experimentally determined μ and μ_{ICRU} . One potential source of uncertainty is our experimental method.

We hence perform a quick check of this by calculating μ of the lead block, the composition of which we know is be consistent with literature, using results obtained using the 10 mm collimator, as seen in figure 6. We compare the expected μ_{Pb} , 1.27 cm^{-1} (see appendix) to our calculated value, $\mu_{\text{Pb TEST}} = (0.74 \pm 0.08) \text{ cm}^{-1}$, finding that $\mu_{\text{Pb TEST}}$ is 42% lower than μ_{Pb} . This result implies a need for major improvements in experimental method (discussed further in section IV.3).

We must also consider that the literature attenuation data available is for modern bone, whereas the bone fragments examined in this work are from the late medieval era. There are multiple factors to consider arising from this half-millennium age difference.

IV.2 Limitations in the Analysis

DMP	m/g	v/cm ³	$\rho_{\approx} / \text{gcm}^{-3}$	$\mu_{\approx} / \text{cm}^{-1}$
1	36 ± 1	45 ± 5	0.79 ± 0.09	0.06
2	54 ± 1	40 ± 4	1.3 ± 0.1	0.1
3	76 ± 1	53 ± 4	1.4 ± 0.1	0.1

Table 2: The mass, m (as measured in the laboratory), volume, v (as estimated by approximating each bone as a hollow cylinder), and approximate density, ρ_{\approx} (calculated from m and v) of each bone fragment, with their resultant predicted attenuation coefficients, μ_{\approx} (the product of approximate bone fragment density ρ_{\approx} and $\mu_{\text{ICRU}}/\rho_{\text{ICRU}}$ from [18]). μ_{\approx} is given to 1 significant figure to reflect uncertainty in ρ_{\approx} .

Modern bones and those from the past will differ due to environmental factors such as diet, disease, and other differences in lifestyle. For example, research has shown that the rate of bone loss in modern women is greater than that of their 18th and 19th century counterparts, potentially due to the more active lifestyle of our predecessors [19]. We can extrapolate this result and assume that bone density would be higher in the late medieval era; however, this result implies that our measured μ should exceed that of modern bone, which it does not.

To account for our low μ , we must also consider the effects of the various decomposition processes undergone by the bone fragments since their burial. Live cortical bone contains osteocytes [6], but in a bone that has undergone approximately 500 years of decay, these cells will no longer be present, leaving behind tiny spaces in the bone's structure. Additionally, Durham Market Place is host to slightly acidic soil [20], which, once in contact with bone, will react with the bone's inorganic bone mineral content, hydroxylapatite. Hydroxylapatite is insoluble but its reaction with acidic soil forms soluble salts, which will then wash away with rainfall or contact with groundwater. Bone is typically composed of 70% hydroxylapatite; in the hundreds of years of mineral content dissolution presumably undergone by DMP1, DMP2 and DMP3, much of this will have been lost, resulting in a substantial decrease in density, and potentially a change in mass attenuation coefficient [21].

We estimate the density of medieval cortical bone by approximating bone fragments as hollow cylinders of cortical

bone, finding values as given in table 2. These ρ_{\approx} are lower than ρ_{ICRU} . It is important to remember that ρ_{\approx} is an approximation, not a true density, as the bones are not perfect cylindrical shells, and are not of uniform composition. Some regions of cortical bone are in fact thicker than others, and others, which for the purposes of the approximation have been assumed hollow, are actually composed of trabecular bone, contributing to the mass from which ρ_{\approx} is calculated. However, these rough values do suggest that the density of medieval bone is lower than that of modern bone, a factor which would contribute to a lower experimental μ .

Notice however that there are still 7%, 32% and 35% differences between μ_{\approx} and experimental μ for DMP1, DMP2 and DMP3 respectively. This is very likely to be the result of experimental error, but could also be due to use of the mass attenuation coefficient of modern cortical bone, $\mu_{\text{ICRU}}/\rho_{\text{ICRU}}$, in the calculation of μ_{\approx} . As previously mentioned, it is very possible that μ/ρ is different for medieval bone, as well as ρ .

As well as deviation from μ_{ICRU} , we also see variation in μ from sample to sample. The range of values yielded may be due to incorrect assumptions about the bone fragments and the images of them taken.

We assume that all bone included in our calculations is cortical, and that all cortical bone has the same ρ and μ (an assumption challenged by our ρ_{\approx} , and other results). These parameters do in fact vary, not only from skeleton to skeleton, but within one skeleton, or even within one bone, due to a wealth of environmental factors including and not limited to the age, sex, diet, and disease.

Despite the variation in μ between samples, the decision was nonetheless made to take the mean, on grounds that the literature values of ρ_{ICRU} and $\mu_{\text{ICRU}}/\rho_{\text{ICRU}}$ referenced in this work are also averages, combining data from various bones of varying ρ and μ .

We assume that x remains as measured at the fragmented end of bone throughout the length of the femur fragment, and that the regions we select for calculation of I_x is solid cortical bone, when in fact we do not know what structures are present where the bone is intact and the interior not exposed (i.e. cortical bone thickness varies along the bone's length, but we assume it is constant).

Flaws in experimental technique will have contributed to both sample-to-sample deviation in μ and discrepancy in μ from its true value (note that, as we have now established, this not necessarily μ_{ICRU}). Whereas for DMP1A and DMP2, an “edge” of pixels corresponding to what was thought to be solid cortical bone is predominantly selected for calculation of I_x , for DMP3, pixels corresponding to almost the whole bone are selected, due to their uniformly low count rate. It is impossible that this whole region is solid cortical bone. We know by inspection that this bone's interior at the sites of fracture is predominantly trabecular and can assume that this continues. This raises questions about the validity of μ for DMP3 as a value for cortical bone, as we know there has been attenuation by multiple media in this case (cortical bone,

cancellous bone, air and dirt trapped between trabeculae). The same can be said for regions of DMP1B. DMP1 is a fragment from the very top of the femur, so is more dominated by cancellous bone. Though we have tried to isolate the cortical bone in this area, there is not an obvious division between trabecular and cortical structure in the images taken, and so the μ calculated may well be for a combination of cancellous and cortical bone, accounting for its lower value.

A lower \bar{N} threshold for pixel inclusion in I_x for DMP3 and DMP1B could facilitate higher definition between solid cortical regions and those of mixed or cancellous composition. Alternatively, employment of a more sophisticated method could allow for easier distinction between bone types.

Ideally, measurements of x would be taken at regular intervals along the bone, with distances between each measurement site corresponding to a pixel on-screen and the direction of measurement aligning exactly perpendicular to the plane of the detector and plane of the Cs-137 source. Each x could then be mapped to its corresponding pixel, and an individual μ for each pixel calculated, still using the average I_0 , but with a location-specific I_x . A map of attenuation coefficient like this could shed more light on the interior structure of the bone, potentially showing the boundary between cancellous and cortical bone. Variation in structure could be identified by pinpointing areas of anomalous μ ; this could indicate an unexpected change in thickness of the exterior cortical bone, the presence of cancellous bone, or maybe even the presence of internal fractures.

For fracture identification, however, incredibly high resolution would be required, which we do not have the time, or the capability to measure x with sufficient accuracy, for. If infeasible to increase resolution sufficiently, the lack of clear edge definition between cortical bone and cancellous bone, and bone and empty space, would remain issues.

IV.3 Limitations of the Experimental Method

In early stages of the experiment, it was hoped that more specific information might be determinable from the imaging results, e.g. information about the individual's age at death, diet, and whether they had been affected by disease. However, the factors that affect bone structure and density are numerous, and even within one skeleton, bones vary greatly, so it is difficult to distinguish one cause for a deviation from the "expected" structure. This would also require definition of an "expected" medieval ρ and μ .

This method has limits in that gamma radiation is unsuitable for imaging samples which may later be analysed using DNA techniques, as irradiation can change the sequence of the DNA. Our bone samples were specifically chosen to be ones which were not planned to undergo any future DNA analysis.

Time was a limiting factor, with each image taking over 20 hours to produce. As a result if this only three bone fragments were imaged, and only incompletely, whereas a larger sample set would have been far more desirable. Given more data collection time, higher resolution images could have been produced, resulting in better definition of (a) the sample's "shadow" from the background and (b) sections of the bones' internal structure, as discussed in section IV.2. This could be achieved via reduction of increment size between points

of measurement, and therefore production of an image with more pixels representing the same physical area. More time would also allow reduction of the collimator aperture size, with longer measurement time at each point so as to still receive enough counts to achieve sufficient contrast.

As the expression for $\alpha_{\bar{N}}$ comprises of terms inversely proportional to N and t , an increased t (and with it, increased N) would reduce $\alpha_{\bar{N}}$ significantly.

The values of $\alpha_{\bar{N}}$ are not displayed in our images for clarity, but are by no means ignored. They are important in the calculation of I_0 , I_x , as these are weighted means, and their errors, α_{I_0} and α_{I_x} (see equations 10 and 11). It is clear from here that μ and its uncertainty α_μ are somewhat dependent on $\alpha_{\bar{N}}$. Lower $\alpha_{\bar{N}}$ would give lower α_{I_0} and α_{I_x} , hence lower $\alpha_{I_0}^\mu$ and $\alpha_{I_x}^\mu$, leading to more precise μ .

The same principle applies to x ; reduction of α_x would also lead to lower α_μ for each bone fragment. Given more time, images from a variety of angles would also have been taken, and x values would be measured at each of these angles, giving a larger data set and reducing standard error.

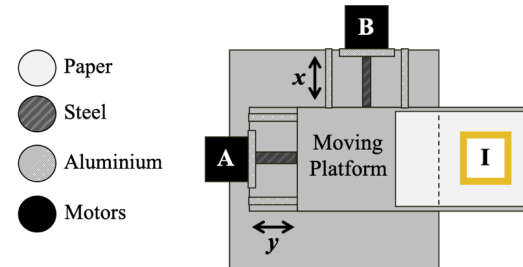


Figure 16: An alternative design for the moving platform, in which an aluminium frame supports a sheet of sturdy paper or other low- μ material, such as a low density wood, onto which the sample is attached in its casing. The sheet of low- μ material would be attached to the aluminium frame by glue, clamps or bolts, depending on its structural integrity.

Aluminium only attenuates gamma very minimally in comparison with shielding materials such as lead (at 661.7 keV, $\mu_{Al} = 0.304 \text{ cm}^{-1}$, whereas $\mu_{Pb} = 1.27 \text{ cm}^{-1}$ [22]). However, the 2 mm thick aluminium platform still reduces gamma ray intensity, i.e. received \bar{N} , by 6% (see appendix for details). This means that to gather a suitable number of counts, more time must be spent measuring at each pixel. This is time that could be spent on obtaining higher resolution, and so higher quality images, giving us the ability to better distinguish bone from background, facilitating increased accuracy in our μ .

An alternative design would replace the protruding section of the moving platform either with a frame-like structure into which sample containers could be attached, suspended with a clamp mechanism such that nothing lay between the sample and the detector. However, this would not be suitable for the fragile nature of the DMP sample set. A more appropriate solution would be the replacement of the aluminium between the sample and detector with a less attenuating material such as paper, as latter depicted in figure 16. However, the structural integrity of paper is a far cry from that of 2 mm of aluminium, and for heavier samples, a more sturdy (but still low- μ) material would be required. One option to investigate

is low density wood. Balsa wood, for example, has $\rho = 0.11\text{-}0.14 \text{ g cm}^{-3}$ [23]. If we assume balsa's mass attenuation coefficient is similar to that of other woods (at 662 keV, $\mu_m \approx 0.08 \text{ cm}^2\text{g}^{-1}$ [24]), $\mu_{\text{BALSA}} = 0.009\text{ - }0.011 \text{ cm}^{-1}$, a third of that of aluminium. A platform of this μ would only cause a 0.2% reduction in gamma intensity, meaning more counts detected per unit time, and so less time required on each pixel.

By including the SCA, we have lost Compton scattering information, and with it potential to determine what proportions of μ are scattering and absorption based. However, as other components of the apparatus scatter, absorb and emit, this data may have been useless.

V Conclusions

We conclude that gamma imaging is a viable technique for archaeological human remains, and that we can reveal information about the structure of a sample, i.e. the gamma images produced in this work confirm that DMP1 and DMP2 are hollow, but suggest that the interior of DMP3 is composed predominantly of cancellous bone. In other words, despite lack of accuracy in determining numerical μ , this method could still be applied as a non-invasive test of the uniformity of a sample's composition, especially at higher resolution.

The average linear attenuation coefficient, μ , for cortical bone in the DMP sample set is found to be $(0.058\pm0.004) \text{ cm}^{-1}$, 61% of μ_{ICRU} , the literature linear attenuation coefficient for modern bone. This discrepancy is largely due to experimental error, but will also have contributions from the differences between modern and archaeological bones, with decay processes having caused changes in ρ , μ_m , and hence μ .

Time constraints restricted the resolution of our images. Higher resolution would not only have yielded more aesthetically pleasing images, but would reduce standard errors and allowed for clearer differentiation between different bone fragment components. Higher intensity radiation, achievable by replacing the aluminium platform extension with a material of lower μ , would result in less time needed to give higher contrast.

VI Acknowledgements

We thank A. Caffell and T. Jakob of Durham University Archaeology Department for their advice and for the kind loan of DMP1, DMP2 and DMP3.

References

- [1] M.F. L'Annunziata, "Radioactivity: Introduction and History," Elsevier BV., Netherlands (2007)
- [2] E. Browne, J. K. Tuli, Nuclear Data Sheets **108** 10 (2007)
- [3] J.J. Rant et. al., "The 8th International Conference of the Slovenian Society for Non-Destructive Testing", Slovenia, 151-155 (2005)
- [4] K. Maher "Basic Physics of Nuclear Medicine/Attenuation of Gamma-Rays," https://en.wikibooks.org/wiki/Basic_Physics_of_Nuclear_Medicine (accessed 27-02-20)
- [5] "L3 Laboratory: High Energy Physics: Imaging with Gamma Radiation," Durham University Physics Department (2020)
- [6] Encyclopaedia Britannica, "Compact Bone," <https://www.britannica.com/science/compact-bone> (accessed 05-04-20)
- [7] Encyclopaedia Britannica, "Cancellous Bone," <https://www.britannica.com/science/cancellous-bone> (accessed 05-04-20)
- [8] G.F. Knoll, "Radiation Detection and Measurement," 4th edition, Wiley, USA (2010)
- [9] "High Purity Germanium Detectors - HPGe," <https://www.nuclear-power.net/nuclear-engineering/radiation-detection/semiconductor-detectors/high-purity-germanium-detectors-hpge/> (accessed 03-04-20)
- [10] I.G. Hughes, T.P.A. Hase, "Measurements and their Uncertainties," Oxford, UK (2010)
- [11] M.O. Miller, SDRP Journal of Earth Sciences & Environmental Studies **3** 4 (2018)
- [12] R.H. Dicke, ApJ **153** (1968)
- [13] D.R. McAlister, "Gamma Ray Attenuation Properties of Common Shielding Materials," Rev. 6 (2018)
- [14] A. Thompson et al., "Centre for X-Ray Optics and Advanced Light Source: X-Ray Data Booklet," LBNL/PUB-490 Rev. 3 (2009)
- [15] E. Arias-Castro, D.L. Donoho, Ann. Stat., **37** 3 (2009)
- [16] R.A. Haddad, A.N. Akansu, IEEE Trans. Signal Process., **39** 3 (1991)
- [17] M.S. Nixon, A.S. Aguado, "Feature Extraction & Image Processing for Computer Vision," Academic Press, UK (2012)
- [18] D.R. White et al., Report 44, ICRU, **os23** 1 (1989)
- [19] B. Lees et al., Lancet, **341** (1993)
- [20] Cranfield University, "Soilscapes soil types viewer - National Soil Resources Institute," <http://www.landis.org.uk/soilscapes/> (accessed 15-04-20)
- [21] U.S. Department of Agriculture, "Preservation of Buried Human Remains in Soil," https://www.nrcs.usda.gov/Internet/FSE_DOCUMENTS/stelprdb1167745.pdf (accessed 15-04-20)
- [22] J.H. Hubbell, S.M. Seltzer, "X-Ray Mass Attenuation Coefficients: NIST Standard Reference Database 126," <https://www.nist.gov/pml/data-xraycoef/index.cfm> (accessed 05-03-20)
- [23] T. Porter, "Wood Identification and Use", Guild of Master Craftsman Publications Ltd. (2004)
- [24] B. Saritha, A.S. Nageswara Rao, J. Phys.: Conf. Ser. 662 012030 (2015)

VII Appendix

VII.1 Information on Radioactive Sources

Source	t / s	$t_{1/2} / \text{s}$
Am-241	$(1.27 \pm 0.01) \times 10^9$	$(1.36 \pm 0.01) \times 10^{10}$
Eu-152	$(5.73 \pm 0.01) \times 10^8$	$(4.27 \pm 0.01) \times 10^8$
Ba-133	$(1.27 \pm 0.01) \times 10^9$	$(3.41 \pm 0.01) \times 10^8$
Na-22	$(6.66 \pm 0.01) \times 10^8$	$(8.20 \pm 0.01) \times 10^7$
Cs-137	$(1.27 \pm 0.01) \times 10^9$	$(9.52 \pm 0.01) \times 10^8$
Co-60	$(1.27 \pm 0.01) \times 10^9$	$(1.66 \pm 0.01) \times 10^8$

Table 3: Ages and half-lives of sources used to calculate the HPGe detector efficiency curve. All information in this table was provided by Durham University Physics Department in [5], with ages and half-lives in years or days to 3 significant figures. We convert these values to seconds for use in our calculations, maintaining this number of significant figures. We use the precision of these values to obtain their uncertainties.

The ages t and half-lives $t_{1/2}$ of the sources used to calculate the HPGe detector efficiency curve are given in table 3. The original activity, A_0 , has the same value for all of the sources used (3.70×10^5 Bq).

VII.2 Shielding Properties of Lead

The $\mu\text{-}\epsilon$ relationship for lead is shown in figure 17, with the relationship fitted around the photopeak energy given by equation 15 with new coefficients e , f , g and h equal to $38.6 \text{ m}^{-1}\text{eV}^{-1}$, 1.00 , $-38.6 \text{ m}^{-1}\text{eV}^{-1}$ and 4.73 m^{-1} respectively. We use the value of the linear attenuation coefficient, μ_{Pb} , yielded by this equation with $\epsilon = 661.7 \text{ keV}$ in calculating the effects of lead shielding on radiation dose rate.

With the constant μ_{Pb} , it is now possible to calculate the effectiveness of our lead shielding, i.e. the amount of radiation it can block. In the following dose rate calculations, values of A_0 , ΣE , A_{0C_o} , ΣE_{C_o} and \dot{N}_{C_o} are as defined in [5]'s example questions.

Dose rate at the interior of the lead shielding is obtained using equation 3 with $X = 0.20 \text{ m}$ to be $\dot{N}_{\text{interior}} = 8.22 \times 10^{-4} \text{ mSvhr}^{-1}$. To find dose rate at the exterior of the lead shielding, equation 1 is employed with $\mu_{\text{Pb}} = 1.27 \text{ cm}^{-1}$ and $\dot{N}_0 = \dot{N}_{\text{interior}}$, resulting in $\dot{N}_{\text{exterior}} = 1.79 \times 10^{-5} \text{ mSvhr}^{-1}$.

VII.3 Shielding Properties of Brass

To verify that the block seen in early imaging tests is brass, we do a quick comparison of the $\mu\text{-}\epsilon$ relationships of its main component, copper (66%), with both lead and cortical bone. Figure 18 shows $\mu\text{-}\epsilon$ for both metals and that for cortical bone, along with an (accidental) image of a brass block and a cortical bone sample. No scale is given but we immediately see the relative contrast, which implies that brass will have a higher μ , as is suggested by its copper dominated composition; it also is immediately obvious from the main plot that copper's attenuation coefficient is closer to that of lead than that of bone. Brass components are therefore clearly non-negligible in the imaging process.

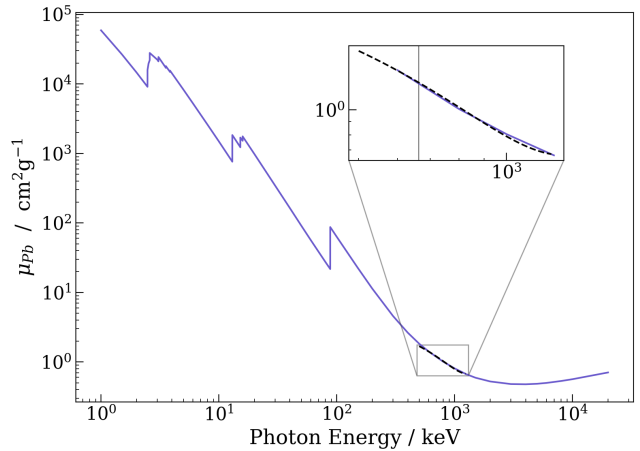


Figure 17: Plots of the linear attenuation coefficient of lead, μ_{Pb} against energy, ϵ . We determine μ_{Pb} by calculating the product of [22]'s values for $\mu_{\text{Pb}}/\rho_{\text{Pb}}$ and $\rho_{\text{Pb}} = 11.35 \text{ gcm}^{-3}$. A fit is applied to the region around 661.7 keV (marked by the solid grey line in the inset) to determine the expected μ at that energy. The dashed black line is the fit, the solid blue the $\mu\text{-}\epsilon$ data. We find $\mu_{\text{Pb}} = 1.27 \text{ cm}^{-1}$.

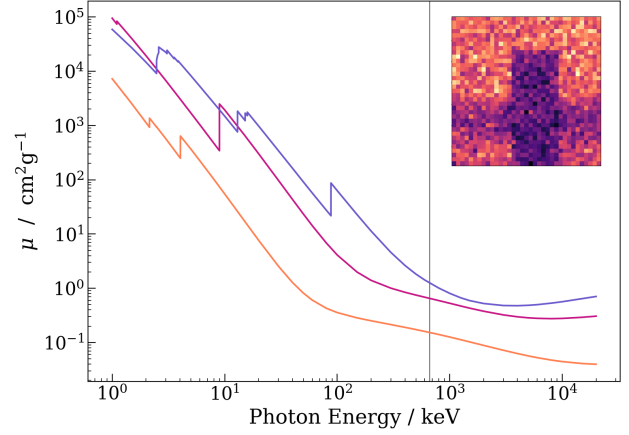


Figure 18: Plots of the linear attenuation coefficients of copper, μ_{Cu} , lead, μ_{Pb} , and cortical bone, μ_{ICRU} , versus ϵ . $\mu_{\text{Cu}}\text{-}\epsilon$ is shown in pink, $\mu_{\text{Pb}}\text{-}\epsilon$ in blue, and $\mu_{\text{ICRU}}\text{-}\epsilon$ in orange. The grey line marks 661.7 keV . Inset is the early imaging test, mentioned previously, showing the brass block (vertical rectangle) and a fox jaw bone (horizontal smudge).

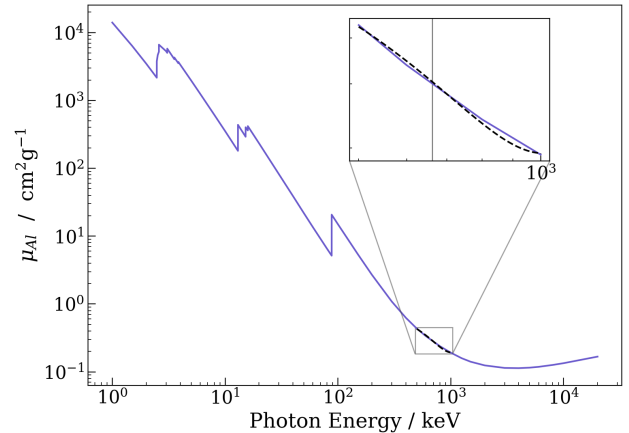


Figure 19: Plots of the linear attenuation coefficient of aluminium, μ_{Al} , against ϵ . We find μ_{Al} in the same way as we did μ_{Pb} , from [22]'s values for $\mu_{\text{Al}}/\rho_{\text{Al}}$, and $\rho_{\text{Al}} = 2.699 \text{ gcm}^{-3}$. The region around 661.7 keV (marked by the solid grey line in the inset) is fitted with a quadratic equation so as to determine the expected μ_{Al} at that energy. Fits are in black, $\mu\text{-}\epsilon$ data in blue. We find $\mu_{\text{Al}} = 0.304 \text{ cm}^{-1}$.

VII.4 Shielding Properties of Aluminium

The $\mu\text{-}\epsilon$ relationship of aluminium is plotted in figure 19, with a quadratic fit in the region surrounding the photopeak energy:

$$\mu = a\epsilon^2 + b\epsilon + c. \quad (16)$$

The values of a , b and c are $(9.08 \times 10^{-7}) \text{ m}^{-1}\text{eV}^{-2}$, $(-1.83 \times 10^{-3}) \text{ m}^{-1}\text{eV}^{-1}$ and 1.12 m^{-1} respectively. From this relationship, we calculate μ_{Al} , the linear attenuation coefficient of aluminium. With this constant known, and via equation 3, an expression for percentage reduction in intensity due to a barrier of aluminium is formulated:

$$\% \text{Reduction} = 1 - \frac{I_x}{I_0} = 1 - e^{-\mu_{\text{Al}}x}. \quad (17)$$

We also use equation 17 to calculate the percentage reduction in intensity of balsa wood, replacing μ_{Al} with μ_{BALSA} .

VII.5 Instrument Details

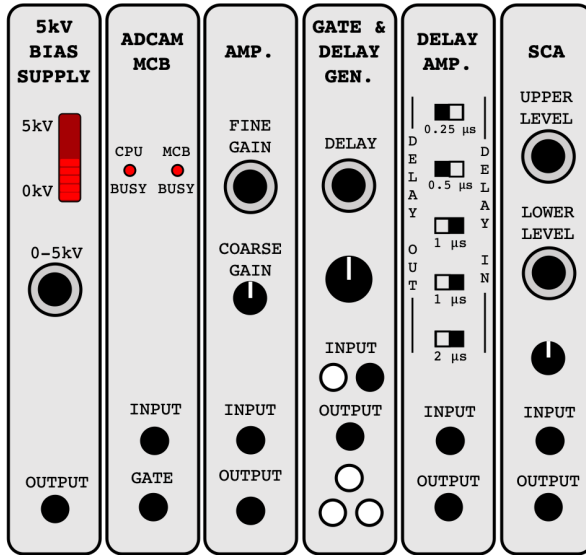


Figure 20: The NIM modules used in the experimental setup, as previously represented as a block diagram. Left to right: ORTEC 659 5kV bias supply, ORTEC 926 ADCAM MCB (interface between HPGe detector and PC), ORTEC 575A amplifier, ORTEC 416A gate generator, ORTEC 427A delay amplifier, ORTEC 550A SCA. The SCA's lower dial determines whether the window produced is symmetric about 0 V.

Figure 20 shows the electronic components of the experimental setup. The HPGe detector take 2.5 kV from the 5 kV bias supply. We set amplifier gain factor, given by the product of fine gain and coarse gain, to approximately 45 in order to achieve our desired spectrum calibration. A delay out of 4 μs is applied using the delay amplifier, and the SCA is set to a window with an upper level of 34 mV. Figure 8 shows how these components are linked.

See overleaf for HPGe detector specifications (figure 21).

VII.6 Data used in Calculation of Attenuation Coefficients

Tables of all count rates and their uncertainties are not provided in this appendix, as even the smallest images, DMP1

DMP	I_0 / s^{-1}	I_x / s^{-1}	$\alpha_{\alpha_{I_0}}^\mu$	$\alpha_{\alpha_{I_x}}^\mu$
1A	1.353 ± 0.001	1.179 ± 0.001	0.0004	0.0005
1B	1.322 ± 0.001	1.164 ± 0.001	0.0004	0.0004
2	1.3670 ± 0.0006	1.1690 ± 0.0007	0.0002	0.0003
3	1.3752 ± 0.0008	1.1676 ± 0.0008	0.0004	0.0004

Table 4: The average count rates, I_0 and I_x , used to calculate attenuation coefficients, μ , for each bone fragment, along with their errors, and magnitude of the contribution of these errors to the error in μ , $\alpha_{\alpha_{I_x}}^\mu$.

A and B, are composed of 1225 pixels. However, table gives all of the weighted mean count rates used in calculations of μ , along with errors and their contributions to the error in μ .

The full versions of the equations for α^μ , mentioned in section IV.1, are as follows:

$$\alpha_x^\mu = \left(-\frac{1}{x + \alpha_x} \ln \left(\frac{I_x}{I_0} \right) \right) - \mu, \quad (18)$$

$$\alpha_{I_x}^\mu = \left(-\frac{1}{x} \ln \left(\frac{I_x + \alpha_{I_x}}{I_0} \right) \right) - \mu, \quad (19)$$

and

$$\alpha_{I_0}^\mu = \left(-\frac{1}{x} \ln \left(\frac{I_x}{I_0 + \alpha_{I_0}} \right) \right) - \mu. \quad (20)$$

VII.7 Units of Fit Parameters

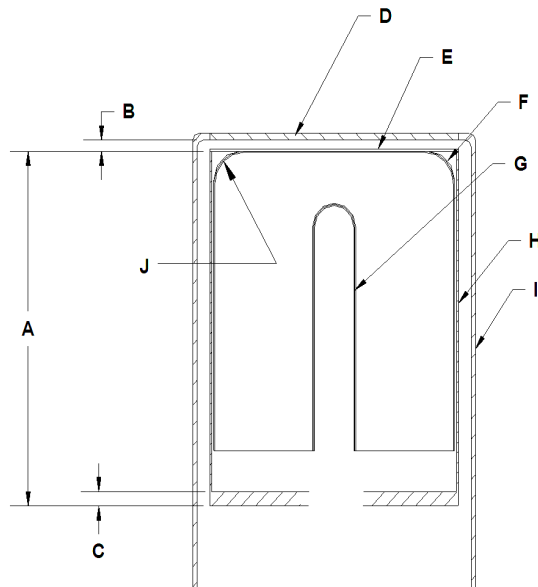
Units of fit parameters are determined by dimensional analysis, e.g. for equation 15:

$$[\mu] = [f][\epsilon]^g + [h][\epsilon] + [i]. \quad (21)$$

We know that $[\mu] = \text{m}^{-1}$ and $[\epsilon] = \text{eV}$. The combination of the units of all the RHS terms must give m^{-1} :

$$m^{-1} = m^{-1} \text{eV}^{-g} \text{eV}^g + m^{-1} \text{eV}^{-1} \text{eV} + m^{-1}. \quad (22)$$

Note: Due to the closure of libraries in response to the COVID-19 pandemic, there has been a greater reliance on department-provided resources such as [5] and online resources e.g. websites, page-limited previews of books on Google Books, and similar.

GERMANIUM DETECTOR DIAGRAM**SERIAL NUMBER 35-TP40602B****COMPANY PRIVATE**

BASIC DETECTOR DIMENSIONS			
DETECTOR DIAMETER	53.3 mm		
DETECTOR LENGTH	43.6 mm		
DETECTOR END RADIUS (J)	8 mm, NOMINAL		
HOLE DIAMETER	10.5 mm		
HOLE DEPTH	31 mm		
HOLE BOTTOM RADIUS	HOLE DIAMETER / 2, NOMINAL		

MISCELLANEOUS DETECTOR ASSEMBLY DIMENSIONS AND MATERIALS			
IDENTIFIER	DIMENSION	DESCRIPTION	MATERIAL(S)
A	94 mm	MOUNT CUP, LENGTH	ALUMINUM
B	3 mm	END CAP TO CRYSTAL GAP	N.A.
C	3.2 mm	MOUNT CUP BASE	ALUMINUM
D	1.3 mm	END CAP WINDOW	ALUMINUM
E	0.03/0.03 mm/mm	INSULATOR/SHIELD	MYLAR/ALUMINIZED MYLAR
F	700 microns	OUTSIDE CONTACT LAYER	Ge with Lithium ions
G	0.3 microns	HOLE CONTACT LAYER	Ge with Boron ions
H	0.76 mm	MOUNT CUP WALL	ALUMINUM
I	1.3 mm	END CAP WALL	ALUMINUM

ORTEC801 S. ILLINOIS AVE.
OAK RIDGE TN 37831**Figure 21:** HPGe Specifications as provided by ORTEC; included here for reference purposes ONLY.